NWP SAF

Satellite Application Facility
for Numerical Weather Prediction

Document No. NWPSAF–EC–TR–007

Version 1.0

May 2002

Microwave radiative transfer modeling in clouds and precipitation Part III: Model Rain and Clouds over Oceans– Comparison with SSM/I Observations

Frédéric Chevallier and Peter Bauer

European Centre for Medium–Range Weather Forecasts

Submitted for publication in Mon. Wea. Rev.

Microwave radiative transfer modeling in clouds and precipitation

Part III: Model Rain and Clouds over Oceans– Comparison with SSM/I Observations

Frédéric Chevallier and Peter Bauer

ECMWF

This documentation was developed within the context of the EUMETSAT satellite Application Facility on Numerical Weather Prediction (NWP SAF), under the Cooperation Agreement dated 25 November 1998, between EUMETSAT and the Met Office, UK, by one or more partners within the NWP SAF. The partners in the NWP SAF are the Met Office, ECMWF, KNMI and Météo France.

Change record			
Version	Date	Author / changed by	Remarks

Contents

Abstract

A comparison of global model cloud and rain parameterization output with satellite observed radiances was carried out. We combined the current operational ECMWF model hydrometeor profiles with a microwave radiative transfer model to generate observation–equivalent radiances simulating the SSM/I measurements. These were generated for two 15–day periods in January and July 2001 to be compared to SSM/I observations from three satellites, namely F–13, F–14, and F–15. The simulations were analyzed to isolate the relative contributions of water vapor, cloud water, rain, and snow to the total signal given their frequency of occurrence in the global fields. The 19.35 GHz channel has the great advantage of being less sensitive to cloud geometry and model generated snow thus providing a more unique relationship between cloud/rain water and TB's. The 37.0 GHz showed great skill in separating cloud and (moderate to heavy) rainfall. The uncertainties in cloud geometry and ice microphysics inhibit an interpretation of 85.5 GHz brightness temperatures.

The evaluation was based on (1) the calculation of cloud and rain occurrence applying the same TB–threshold screening to both observations and simulation; and (2) the analysis of global TB–histograms for clouds and precipitation. From the first part, the model tendency to produce too large cloud and rain systems was identified. While some smaller scale cloud features are missing, the onset of condensation generally produces larger systems than observed. Since the precipitation scheme is diagnostic, the cloud scheme propagates this problem to the rain coverage. With the results from the second part, the overestimation of extent and intensity was quantified to ≈10–15 K at 19.35 and ≈15–30 K at 37.0 GHz at horizontal polarization.

This was consistent with a direct estimation of retrieved liquid water paths using a variational retrieval scheme and of rainfall rates from a parametric algorithm. The globally averaged liquid water path from the model's first–guess was about 75% higher than that from the retrievals while globally averaged rainrate was 160% higher than retrieved. The major contribution to this overestimation originated from the tropics suggesting the convection scheme and/or its inputs as a major source of overestimation.

1 Introduction

As radiometers do not directly measure the atmospheric constituents, two approaches co–exist for the comparison of model and satellite data. Either the observations are converted to model variables (satellite–to–model approach) or synthetic observations are computed from the model parameters (model–to–satellite approach). Each of the two possibilities is affected by different spatial and temporal sampling and resolutions of model data vs. observation. Observations represent an integration of information contributions from several sources, i.e., emission and scattering of electromagnetic radiation by surface and atmospheric constituents. Thus the observable–parameter relationship may not be unique and discrepancies between models and observations difficult to interpret.

For model evaluation purposes, the model–to–satellite approach tends to be favored because retrieval errors are usually difficult to characterize (e.g., Morcrette 1991, Rizzi 1994, Shah and

Rind 1995, Roca *et al.* 1997, Chaboureau *et al.* 2000, Chevallier *et al.* 2001). Therefore both elements of the comparison may be erroneous or at least seriously biased. This aspect is even more important for the assimilation of satellite data and therefore operational weather centers progressively turn to the direct assimilation of radiances instead of retrieved products (e.g., Andersson *et al.* 1994, Derber and Wu 1998). Aiming at the assimilation of rain–affected radiances, however, it has to be verified that the model clouds can realistically represent observable radiances in terms of grid–averaged cloud geometry and microphysical properties.

This study represents one of the first attempts to characterize the quality of global model precipitation schemes employing the precipitation signature in radiance space. The model–inherent radiation schemes generate radiation budget elements (shortwave and longwave, i.e., wavelengths of 0.3–4μm and 4–40μm) which are historically compared to earth radiation budget observations from satellites (e.g. Cess et al. 1997) but which only provide information relevant to bulk non–precipitating cloud parameters. Precipitation analyses, however, require the simulation of microwave radiative transfer in the model atmosphere to be compared to available satellite data. Here, the availability of a sophisticated global operational model with simulation scales of the same order as satellite observations provides a unique tool to evaluate the model cloud physics over all synoptic regimes.

Our starting point is therefore the description of observational and model data used for the intercomparison as well as a description of the microwave radiative transfer model (Section 2). Section 3 begins with a description of the relative information contributions of water vapor, clouds, and precipitation to the simulated radiances. The evaluation is based on (1) the frequency of precipitation occurrence in both model and observations and (2) the analysis of radiance probability density functions (pdf's). The latter are interpreted by use of the information content previously outlined and on the basis of both global data sets and regional case studies. Methodology and results are summarized and general conclusions are drawn in Section 4.

2 Data sources

2.1 Satellite data

The Special Sensor Microwave / Imager (SSM/I) passive microwave radiometer is operated since 1987 on–board the Defense Meteorological Satellite Program (DMSP) satellites with a near–circular, sun–synchronous, and near–polar orbit. SSM/I's imaging is carried out on a conical scan thus constant surface zenith angle (53.1 degrees) and at four frequencies (19.35, 22.235, 37.0, and 85.5 GHz) with dual polarization, except at 22.235 GHz where only vertically polarized measurements are available. The size of the instantaneous field of view decreases with frequency. The spatial resolution of the 19.35, 22.235, and 37.0 GHz channels (63×49, 50×40, and 37×28 km^2, respectively) is comparable to the resolution of the ECMWF forecast model (40×40 km^2), but the 85.5 GHz channel resolution, 15×13 km^2, is significantly higher (Hollinger *et al.* 1987). Orbit altitude and active scan angle provide a swath width of about

Observation time (UTC)	03:00	06:00	09:00	12:00	15:00	18:00	21:00	24:00
Forecast range (hours)	3	6	9	12	3	6	9	12

Table 1: Forecast ranges used here for the simulation of the SSM/I TB's.

1,400 km.

For the purpose of this study, two periods of 15 days were selected: January 1–15 and July 1–15, 2001. In both cases, observations from three DMSP satellites, F–13, F–14 and F–15, were employed over oceans after screening of sea–ice. Since the F–13, F–14 and F–15 orbits have a descending node time of approximately 0600, 0900, and 0730 LST and an ascending node time of approximately 1800, 2100, and 19:30 LST global coverage is achieved during one day.

2.2 Model data

Model profiles (temperature, specific humidity, cloud cover, liquid water, ice water, rain and precipitating snow) and surface characteristics (pressure, temperature and wind) were extracted from the ECMWF archives with a temporal resolution of three hours over the two 15–day periods. As a consequence, observations and model data are collocated within 1.5 hours. The reference observation times and the corresponding forecast ranges are summarized in Table 1. The data were produced by cycle 23r4 of the ECMWF forecast system, the characteristics of which are summarized hereafter.

Analyses are produced at nominal times of 00 and 12 UTC by the 4–dimensional variational (4D–Var) data assimilation system described by Courtier *et al.* (1994), with an assimilation window of 12 hours. Pressure, temperature, water vapor, and wind information are obtained from conventional and satellite observations. Of relevance to the present study is that SSM/I observations are assimilated in the form of retrieved total water vapor content and retrieved 10–meter wind speed over oceans in non–rainy areas (Gérard and Saunders 1999). The temperature of the sea surface is prescribed with the National Center for Environmental Prediction (NCEP) analyses output.

The forecast model is a global spectral $T_L511L60$ model. It includes a semi–Lagrangian advection scheme together with a linear Gaussian grid (Hortal 1999). The reduced horizontal grid corresponds to a regular grid size of about 40 *km* from the equator to the poles. In the vertical, a hybrid coordinate of 60 levels between the surface and the top of the atmosphere is used. The physics package is an improved version of that described by Gregory *et al.* (2000), with the main modifications summarized by Jakob *et al.* (2000) and Morcrette *et al.* (2001). In particular, two prognostic equations describe the time evolution of cloud condensate and cloud cover, while rain and snow are diagnostic quantities. Jakob (2000) describes the modifications to the original formulation from Tiedtke (1993). Clouds are formed by convection, diabatic cooling and boundary–layer turbulence. The scheme links their dissipation to adiabatic and diabatic heating, turbulent mixing of cloud air with unsaturated environmental air, and pre-

cipitation processes. Precipitation processes are parameterized in the convection scheme and in the stratiform cloud scheme and are computed in terms of rain and snow precipitation rates, with units $kg(m^2\,s)^{-1}$. In pure ice clouds, the generation of precipitation is treated as a sedimentation process of cloud ice following Heymsfield and Donner (1990). The parameterization uses a formulation following Sundqvist (1978) in mixed–phase and water clouds. Rain and snow fall out and evaporate consistently with the cloud overlap (Jakob and Klein 2000).

2.3 Radiative transfer model

The computation of model–equivalent SSM/I radiances (expressed as blackbody equivalent brightness temperatures, TB's) is based on a two–stream Eddington approximation model assuming plane–parallel atmospheres (Bauer *et al.* 1998, Bauer 2002, Moreau *et al.* 2002). When compared to more accurate multiple–stream or Monte Carlo models, model uncertainties remain below 1–2 K in most situations at SSM/I frequencies (Smith *et al.* 2002).

The hydrometeor optical properties (i.e. the extinction coefficient, the single scattering albedo, and the asymmetry parameter) are provided to the radiation model from pre–computed Mie–tables for liquid water, cloud ice, rain and precipitating ice (Bauer 2001). The conversion from rain and snow rates (as archived from the forecast model) to water contents (as used by the radiative transfer model) is carried out in agreement with the Mie computations assuming standard size distributions and fall speeds of the hydrometeors (Bauer 2001). Extinction coefficients for oxygen and water vapor were obtained from the Millimeter Propagation Model (Liebe *et al.* 1992).

Polarization is only introduced by the sea surface properties. The latter are obtained in terms of an effective emissivity and an effective reflectivity from the FASTEM–2 model (English and Hewison 1998, Deblonde and English 2000), that accounts for non–specular reflection by a wind roughened sea–surface within a simple and computationally efficient formulation. The validation of FASTEM–2 shows that the model uncertainty in terms of apparent surface temperature is of the order of 1 K. It is obvious that the impact of FASTEM–2 errors on the TB–computation decreases with increasing atmospheric opacity. Polarization may also originate from radiance scattering at spherical and non–spherical particles (Prigent *et al.* 2001). However, given the rather coarse microphysical detail resolved by global model cloud schemes the neglection of scattering–induced polarization seems of minor importance compared to uncertainties of the hydrometeor profiles and cloud coverage parameterization.

The geometry of the hydrometeor profiles in the forecast scheme is rather complex. Indeed, fractional cloud cover and fractional precipitation cover are defined separately in each atmospheric layer. The cloud layers are overlapped following a maximum–random approximation. Precipitation is distributed in the vertical in consistence with the corresponding cloud geometry and the model physics. In order to reduce the computing time of the radiative transfer code for the present study, the geometry of the one–dimensional profiles was simplified in the TB calculations. Firstly, the fractional cloud cover was assumed to be constant in the vertical, with maximum overlap of the cloud layers. The cloud cover for the radiation scheme was chosen as

the maximum value of the cloud cover in the liquid water layers provided by the forecast model. Scattering was introduced in the cloudy part of the grid only. The clear and cloudy radiance streams are linearly combined to obtain the final TB but they do not interact. Secondly, precipitation coverage is assumed to be equal to the cloud coverage, without any distinction between convective rain and stratiform rain. This simplification of the geometry is not expected to introduce errors in excess of a few K since microwave radiation is sensitive to large amounts of hydrometeors only, for which the cloud cover and precipitation cover are usually close to unity in the forecast model. However, larger errors may occur at the boundaries of cloud systems.

The uncertainty of the total radiance computation is difficult to quantify because the impact of the simplified geometry is hard to verify. However, given the above estimates a total TB–uncertainty of about 3 K at 19.35, 22.235, and 37.0 GHz and 3–5 K at 85.5 GHz seems reasonable. Of these, the cloud geometry approximation and the sea surface emissivity model clearly dominate the error budget.

3 Comparison

The first part of the evaluation is dedicated to the representation of precipitation occurrence in both model simulations and observations. An objective rain identification is introduced in TB–space rather than on hydrometeor level. This is because rain parameterization schemes tend to produce too much very small precipitation rates. In that case, an artificial cut–off of erroneously low parts of rain pdf's would have to be used. Therefore, the rain flags of Stogryn *et al.* (1994) have been implemented here which identify clouds by the increasing depolarization generated by sea–surface reflection at 37.0 GHz, i.e., $T_{37V} - T_{37H} \leq 50\ K$, and rain if the lower frequency TB's exceed certain thresholds, i.e., $T_{19V} \geq T_{37V}$ or $T_{19H} > 185\ K$ or $T_{37H} > 210\ K$.

Clouds and rain are irregularly spread in the atmosphere and form structures of which the horizontal scale varies by several orders of magnitude. A slight displacement (two grid points, for instance) of a frontal system in the atmospheric model with respect to observations will significantly degrade a point–by–point comparison. In the present case, 115,514 (respectively 253,620) rain–affected grid points were detected in the SSM/I observations (respectively in the model) between January 1 and 15 using the above rain flags. Despite the twofold overestimation of the number of rain–contaminated point by the model, only 64,814 grid points are rainy in both model and observations. Small mislocations of the systems and the width of the collocation time window (1.5 hour, see section 2.2) explain this number. As a consequence, point–by–point comparisons would be misleading here. The present validation is thus based on rain and cloud frequency of occurrence as well as on TB–pdf's over the two 15-day periods.

3.1 Information content of the SSM/I observations

In order to assess the contribution of various atmospheric variables to the SSM/I TB's, a sensitivity study was performed with the data from January 1. For the 8,232 rain–affected model

profiles available over ocean, equivalent SSM/I TB's were computed by adding successively the constituents cloud liquid water, rain, and snow to the clearsky model profiles. No computation was made for the contribution of cloud ice since it does not significantly affect the SSM/I channels. The impact of the atmospheric variables on the TB pdf's is presented in Figure 1 for each of the seven channels.

Water vapor is the main contributor to the clear atmosphere emission in all SSM/I channels due to water vapor continuum absorption and a strong absorption line at 22.235 GHz. Since continuum absorption increases with frequency, the 85.5 GHz 'window' channel shows a similar sensitivity to water vapor as the 22.235 GHz channel. Liquid water absorption and scattering increases with frequency as well. All histograms (W+L) therefore show a shift to higher TB's indicating more opaque atmospheres above the radiometrically cold ocean background. Adding rain (W+L+R) produces another shift to higher TB's between 19.35 and 37.0 GHz since rain drop absorption is stronger than scattering. However, at 85.5 GHz scattering becomes important and TB's decrease. Finally, by adding snow (W+L+R+S) only little effect is observed at 19.35 and 22.235 GHz while scattering dominates at 37.0 and even stronger at 85.5 GHz.

Since the addition of both cloud liquid water and rain tend to produce a shift of pdf's in the same direction, light rain would be difficult to separate from cloud liquid water (e.g., Bauer *et al.* 2001). Another aspect is the sensitivity to cloud structure. With increasing frequency the cloud transmission is reduced thus higher levels dominate the signal. Therefore the higher frequency signals depend more strongly on the vertical liquid and ice water distribution while the 19.35 and 22.235 GHz channels mainly respond to the integrated water path. When simulations are compared to observations the differences will then be driven by different rain column depths and average rain water contents (or rainrates) in that column.

3.2 Frequency of occurrence

The frequency of occurrence of liquid clouds (non–raining and raining) for January and July is shown in Figure 2. The results exhibit some of the main patterns of the atmospheric general circulation: The intertropical convergence zone (ITCZ), the South Pacific convergence zone (SPCZ) and the mid–latitude storm tracks. The cloud detection used here is too restrictive to display the liquid clouds of the descending–motion regions, such as the cumulus trade winds and the stratocumulus regions off the west coast of the continents. Consistent with previous validations of the ECMWF model (e.g. Chevallier *et al.* 2001), the patterns are shown to be well reproduced on the short forecast ranges considered with respect to observations. However, the model overestimates the frequency of occurrence in most regions, in particular in the storm tracks, in the Atlantic ITCZ and in the east Pacific ITCZ.

Figure 3 displays the frequency of occurrence of rain for the two 15–day periods. As expected, it exhibits the same regions as for the clouds (Figure 2), but with thinner structures. The observed structures are also remarkably well located by the model, but they are too large and too intense. Even though the model spatial resolution is high the generated cloud structures do not well represent small–scale convection and organized mesoscale convection. Once

convection is initiated it will have a tendency to contaminate adjacent grid boxes and thus overestimate the extent of observable clouds.

3.3 Probability density functions

TB–pdf's are presented in Figures 4 and 5 for January and July, respectively. In order to focus on the rain areas they were restricted to those grid points where rain was detected in either observation or model at least once over the whole 15-day period. These were the points reproduced in the shaded areas in Figure 3.

Generally, two peaks can be distinguished in the pdf's which reflect the general difference between mid–latitude and tropical temperature regimes. The magnitude of the cold peak is larger inasmuch as the number of mid–latitude points is higher as can be seen in Figure 3. The shape of the distributions and the differences between the model and the observations are similar for the two polarizations. However, the model's coldest TB's, therefore cloud–free, appear to be biased warm by a 2–3 K in the 19.35, 22.235, and 37.0 GHz vertically polarized channels. This is not the case in the corresponding horizontally polarized channels and is likely to reflect a bias produced by the surface emissivity model.

The number of occurrence of the highest TB's at 19.35 and 37.0 GHz, which are therefore generated by cloud and possibly rain emission, is higher in the model simulations than in the observations. This is consistent with the results of Figures 2 and 3 that exhibited an overestimation of cloud and rain occurrence in general. Furthermore, it may indicate an overestimation of the rain intensity (and/or of the cloud liquid water paths) for most precipitating cases since the rain layer depth will be rather well reproduced due to its close correspondence to freezing level altitude.

For clear cases, the 22.235 GHz model pdf fits the observed one particularly well (not shown here) which indicates the good representation of water vapor in the model shortrange forecast. This is not surprising since thinned SSM/I observations of total water vapor path are operationally assimilated in clear areas. However, in the situations collected here (i.e. with at least one rain contamination per two–week period) some differences occur. Firstly, the model has a cold bias in the Tropics (at around 260 K in Figures 4c and 5c). Owing to the positive biases from the emissivity model and the model cloud liquid water which were noticed at 19.35 and 37.0 GHz, this may indicate a lack of water vapor in the tropical convective systems, that could be explained further by a cold temperature bias in these areas. Secondly, the model has a warm bias in mid–latitudes, in particular in boreal summer likely because of excessive cloudiness along the storm tracks, as was seen in Figure 2.

Comparing Figures 4 and 5 some seasonal variation can be observed. In July, the Pacific ITCZ is intensified and the Indian Ocean monsoon is active while SPCZ is less well defined. Over the Southern oceans rainfall patterns are generally more widespread and precipitation is more intense. Also, smaller scale features like the rain maximum over the Gulf and Kuroshio streams are well expressed in July. More atmospheric humidity in tropical atmospheres is reflected in the change of magnitude of TB peaks at 22.235 GHz (Figure 4c vs. 5c). Also those

Region	w_{FG} $[kg\,m^{-2}]$	w_{RET} $[kg\,m^{-2}]$	RR_{FG} $[mm\,h^{-1}]$	RR_{RET} $[mm\,h^{-1}]$
global	0.115	0.064	0.151	0.058
mid–latitudes	0.108	0.075	0.133	0.057
tropics	0.124	0.054	0.181	0.060

Table 2: Averaged cloud liquid water contents (w) and rainrates (RR) from model first–guess (FG) and retrievals (RET) for period January 1–15, 2001.

peaks at 19.35 GHz associated to precipitation are amplified by enhanced tropical convection (Figure 4a,b vs. 5a,b) and also the peak at larger TB's at 37.0 GHz is more pronounced in July (Figure 4d,e vs. 5d,e).

To separate between cloudy and rainy cases which were accumulated in Figures 4 and 5, the same pdf's were reproduced only containing rainy cases. Therefore those samples were selected for Figure 6 where either model or observation showed rain (here only shown for January 2001). The sample sizes were 304,320 for January and 322,804 for July. It is noteworthy that in January, 890,839 samples were classified as cloud/rain contaminated from the model and 763,929 from the observations. This quantifies the observation from Figure 2, i.e., the model rain areas are larger than those observed. Together with Figure 1, Figure 6 can give some information on model deficiencies. For instance, Figure 6b indicates the excess cloud occurrence and cloud liquid water / rain amounts in the model simulations. The histogram is shifted to the right and the difference between clouds and rain (which is identified by the small side–peak in the observations) disappeared. The shift at lower TB's reaches ≈10–15 K at 19.35 and ≈15–30 K at 37.0 GHz at horizontal polarization. Since both shifts are positive and cloud absorption increases linearly with frequency they are most likely associated with cloud water rather than precipitation.

The 85.5 GHz channel provides information on precipitating ice since the scattering at large ice particles significantly reduces the TB's. From Figures 4–6f and g, the model appears to produce shallower pdf's at 85.5 GHz than the observations. So there are both cases where the model generates too much precipitating ice, and cases where it does not produce enough. Deeper analysis of the results shows that the excessive production mainly occurs in the mid–latitude storm tracks. Further investigation would be particularly interesting because the model is known to generally lack cloud ice water, in particular in the mid–latitudes (Chevallier *et al.* 2001). Validation of the ice fallout scheme would therefore help analyzing the causes of this deficiency. However, such a study is hampered by the lower accuracy of the radiative transfer simulations at 85.5 GHz and by the resolution difference between the atmospheric model and the observations (see Section 2.1).

A means of quantifying the model bias in TB is the comparison of the model first–guess liquid water path, w, with that of the one–dimensional variational retrieval (Phalippou 1996)

which is operationally generated at ECMWF along with water vapor path and near–surface windspeed. This only applies to non–precipitating situations in the observations. The three panels in the left column of Figure 7a show the w–pdf's over the period January 1–15 2001 comparing the model first–guess with the variational retrieval (1D–Var) for all data, mid–latitudes (30–60N, 30–60S), and the tropics (30S-30N). The right–column panels show a similar comparison of near–surface rainrates between model first–guess and those obtained from the SSM/I rain retrieval algorithm of Bauer and Schlüssel (1993). Table 2 summarizes the averaged water contents and rainrates, respectively.

The model shows the tendency to globally overestimate liquid water path above $w = 0.03 kg\,m^{-2}$. The magnitude of overestimation amounts to 44% in the mid–latitudes and to 131% in the tropics which reduces to 79% globally. Since the model's rain parameterization is diagnostic, this trend is propagated to the rain production as well. Therefore, a global overestimation of 160% is observed, i.e., 134% in the mid–latitudes and 200% in the tropics. The rainrate–pdf of the observations drops off fairly quickly for $RR < 0.4 mm/\,h^{-1}$ because a lower threshold for rain detection was used with the Bauer–Schlüssel algorithm.

The overestimation is very dramatic and is far above the expected uncertainty of the retrievals. Also, it is only partly explained by an overestimation of cloud/rain area extent. It also confirms the previously outlined performance in TB–space. Since the contribution of convective systems to total cloud occurrence and rainfall is larger in the tropics than in mid–latitudes, the convection scheme and/or its input data, e.g. temperature (as discussed above), may be mainly responsible for the overproduction of liquid water that later becomes precipitation.

3.4 Individual cases

Some individual cases from January 2001 are shown separately in Figure 8 for the Northern Atlantic and in Figure 9 for the Indian Ocean (TB's at 19.35 GHz, horizontal polarization). The highest TB's indicate rain areas, whereas the lowest TB's correspond to cloud–free scenes. The figures corroborate the information gained from the 15–day statistics: The convective systems are well located, in particular in the mid–latitudes, which indicates the good performance of model dynamics. However, the systems are too intense, both in terms of rain and in terms of cloud liquid water.

The extent of the frontal systems are nicely depicted in both observations and model fields (Figure 8). As previously mentioned, the model simulations exhibit more intense rainfall in the updraft regions while some smaller scale features in the warm sectors are missing. The intensity difference is again expressed by TB–differences of $\approx$20.0 K.

In the Indian Ocean (Figure 9) two tropical cyclones can be identified which were 'Ando' on January 7, South–East of Madagascar and 'Bindu' on January 11, East of Madagascar. It is interesting to notice the improvement of the representation of the tropical cyclones between previous studies (e.g. Marécal and Mahfouf 2000, 2002) and the current model version. Both shape and intensity of 'Ando' and 'Bindu' are much better simulated than were 'Anacelle' and 'Bonnie' (both in 1998). This is a consequence of an increase of forecast model resolution from

60 *km* to 40 *km* even though it is still not sufficient for the development of an inner eyewall as observed on January 11 (Figure 9e vs. 9f).

4 Discussion

Satellite observations have been providing valuable information on cloud profiles generated by the ECMWF model, in particular in recent years (Jakob 1999, Klein and Jakob 1999, Chevallier and Morcrette 2000, Chevallier et al. 2001, Chevallier and Kelly 2002). This paper extends the scope of these studies to the model precipitation profiles.

When evaluating global model cloud and rain parameterization schemes with satellite data, a comparison in radiance space seems favorable since the retrieval of bulk cloud and rain microphysical quantities from observations is rather difficult. This is in particular true for near–surface rainfall rate or hydrometeor concentration profiles. For this reason, we combined the current operational ECMWF model hydrometeor profiles with a microwave radiative transfer model to generate observation–equivalent radiances simulating the SSM/I measurements. With this approach, the error sources are restricted to the assumptions made for cloud geometry and particle size distributions (which are also inherent to physical retrieval algorithms) and the models used for surface emissivity and radiative transfer calculations. The latter are comparably easy to quantify and amount to a few K depending on frequency and polarization.

Observation–equivalent simulations were generated for two 15–day periods in January and July 2001 to be compared to SSM/I observations from three satellites, namely F–13, F–14, and F–15. In a first step, the simulations were analyzed to isolate the relative contributions of water vapor, cloud water, rain, and snow to the total signal given their frequency of occurrence in the global fields. The SSM/I 19.35 GHz channel has the great advantage of being less sensitive to cloud structure and to model generated snow thus providing a more unique relationship between cloud/rain water and TB's. Both cloud and rain could be separated by the superposition of gross emission and occurrence at 37.0 GHz (horizontal polarization), that is TB–histograms showed a cloud–related maximum at 220 K and a rain–related maximum at 250 K. It was evident that rainfall with low intensity would be difficult to distinguish from non–precipitating clouds. In any case, the influence of water vapor is dominant since almost all observations/simulations contain clear–sky contributions. Snow mainly drives the signal at 85.5 GHz but model cloud ice microphysics, cloud geometry vs. SSM/I footprint size, and snow particle size distribution are very uncertain so that the comparison of TB's would be difficult to interpret.

The evaluation was based on (1) calculation of cloud occurrence applying the same TB–threshold screening to both observations and simulation; and (2) the analysis of global TB–histograms for clouds and precipitation. From the first of them, the model tendency to produce cloud and rain systems which are too large was identified. While some smaller scale features are missing, the onset of condensation will generally produce larger systems than observed. Since the precipitation scheme is diagnostic, the cloud scheme will propagate this problem to the rain coverage. From the histogram comparison, the overestimation of extent and intensity was quantified to ≈10–15 K at 19.35 and ≈15–30 K at 37.0 GHz at horizontal polarization at

the lower end of the TB dynamic range.

In summary, our evaluation confirms previous results from Chevallier *et al.* (2001) using AMSU data concerning the model tendency to overestimate cloud extent and liquid water path. The SSM/I observations indicate an analogous behavior for the model's rain production resulting in TB–biases between 10–30 K at SSM/I frequencies. This has to be interpreted as the sum of cloud and rain contributions to the signal since the water vapor contents and surface winds are already strongly constrained through the assimilation of SSM/I observations in non–precipitating areas. The above comparison already suggests the convection scheme as a starting point.

The analysis introduced above forms the basis for a possible direct usage of cloud and rain–affected radiances in the assimilation system. This would represent an alternative with respect to the assimilation of rainrates (e.g. Marécal and Mahfouf 2002). The advantages of assimilating radiances are the better knowledge of forward modeling errors as well as the independence of algorithm training data sets which are known to lack global representativeness. On the other hand, the present study depicts the deficiencies of the model first guess bulk cloud parameters which may represent a handicap within the variational assimilation framework.

Acknowledgements

The authors gratefully acknowledge the support by E. Moreau for the evaluation of the radiative transfer calculations. We are also indebted to V. Marécal, Jean–François Mahfouf, Jean–Noël Thépaut, Martin Miller, and Tony Hollingsworth for numerous discussions on the subject.

References

Andersson, E., J. Pailleux, J.-N. Thépaut, J.R. Eyre, A.P. McNally, G.A. Kelly and P. Courtier, 1994: Use of cloud–cleared radiances in three/four–dimensional variational data assimilation. *Q. J. Roy. Meteor. Soc.*, **120**, 627–653.

Bauer, P. and P. Schlüssel, 1993: Rainfall, total water, ice water and water–vapour over sea from polarized microwave simulations and SSM/I data. *J. Geophys. Res.*, **98**, 20737–20759.

Bauer, P., L. Schanz, and L. Roberti, 1998: Correction of three–dimensional effects for passive microwave remote sensing of convective clouds. *J. Appl. Meteor.*, **37**, 1619–1632.

Bauer, P., 2001: Including a melting layer in microwave radiative transfer simulation for clouds. *Atmos. Res.*, **57**, 9–30.

Bauer, P., P. Amayenc, C,D Kummerow, and E.A. Smith, 2001: Over–ocean rainfall retrieval from multisensor data of the Tropical Rainfall Measuring Mission. Part II: Algorithm implementation. *J. Atmos. Oceanic Technol.*, **18**, 315–330.

Bauer, P., 2002: Microwave radiative transfer modeling in clouds and precipitation. Part I: Model description. *NWP SAF Report No. NWPSAF-EC-TR-006*, 27 pp.

Cess, R.D., and co–authors, 1997: Comparison of the seasonal change in cloud–radiative forcing from atmospheric general circulation models and satellite observations. *J. Geophys. Res.*, **102**, 16593–16603.

Chaboureau, J.–P., J.–P. Cammas, P. Mascart, J.–P. Pinty, C. Claud, R. Roca, and J.–J. Morcrette, 2000: Evaluation of a cloud system life–cycle simulated by Meso–NH during FASTEX using METEOSAT radiances and TOVS–3I cloud retrievals. *Q. J. Roy. Meteor. Soc.*, **126**, 1735–1750.

Chevallier, F., and J.–J. Morcrette, 2000: Comparison of model fluxes with surface and top–of–the–atmosphere observations. *Mon. Wea. Rev.*, **128**, 3839–3852.

Chevallier, F., P. Bauer, G. Kelly, C. Jakob, and T. McNally, 2001: Model clouds over oceans as seen from space: Comparison with HIRS/2 and MSU radiances. *J. Climate*, **14**, 4216–4229.

Chevallier, F., and G. Kelly, 2002: Model clouds as seen from space: comparison with geostationary imagery in the 11 μm channel. *Mon. Wea. Rev.*, in press.

Courtier, P., J.–N. Thépaut, and A. Hollingsworth, 1994: A strategy, for operational implementation of 4D–Var, using an incremental approach. *Q. J. Roy. Meteor. Soc.*, **120**, 1367–1388.

Deblonde, G., and S.J. English 2000: Evaluation of the FASTEM-2 fast microwave oceanic surface emissivity model. *Proceedings of the Int. TOVS Study Conference, Budapest, Hungary, 20–26 September 2000,* 67–78.

Derber, J. C., and W.–S. Wu, 1998: The use of TOVS cloud–cleared radiances in the NCEP SSI analysis system. *Mon. Wea. Rev.*, **126**, 2287–2302.

English, S., and T.J. Hewison, 1998: A fast generic millimetre wave emissivity model. In *Proceedings of the International Society for Optical Engineering (SPIE) on Microwave Remote Sensing of the Atmosphere and Environment*, T. Hayasaka, D.L. Wu, Y.–Q. Jin, J.–S. Jiang

(Eds.), **3503**, 22–30.

Gérard, É., and R. Saunders, 1999: Four–dimensional variational assimilation of Special Sensor Microwave/Imager total column water vapor in the ECMWF model. *Q. J. Roy. Meteor. Soc.*, **125**, 3077–3101.

Gregory, D., J.–J. Morcrette, C. Jakob, A.C.M. Beljaars, and T. Stockdale, 2000: Revision of convection, radiation and cloud schemes in the ECMWF Integrated Forecasting System. *Q. J. Roy. Meteor. Soc.*, **126**, 1685–1710.

Heymsfield, A.J. and Donner, L. J., 1990: A scheme for parameterizing ice–cloud water content in general circulation models. *J. Atmos. Sci.*, **47**, 1865–1877.

Hollinger, J.P., R.C. Lo, G. A. Poe, R. Savage, and J.L. Pierce, 1987: Special Sensor Microwave/Imager User's Guide. Naval Research Laboratory, Washington D.C., 177 pp.

Hortal, M., 1999: The development and testing of a new two–time–level semi–Lagrangian scheme (SETTLS) in the ECMWF forecast model. ECMWF Technical Memorandum No. 292 [available from ECMWF, Shinfield Park, Reading, Berks. RG2 9AX, UK].

Jakob, C., 1999: Cloud cover in the ECMWF reanalysis. *J. Climate*, **12**, 947-959.

Jakob, C., 2000: The representation of cloud cover in atmospheric general circulation models. *PhD thesis*, Ludwig-Maximilians–Universität München, 193 pp.

Jakob, C., E. Andersson, A. Beljaars, R. Buizza, M. Fisher, E. Gérard, A. Ghelli, P. Janssen, G. Kelly, A. P. McNally, M. Miller, A. Simmons, J. Teixeira, and P. Viterbo, 2000: The IFS cycle CY21r4 made operational in October 1999. *ECMWF Newsletter*, **87**, 2–9.

Jakob, C., and S.A. Klein, 2000: A parameterization of the effects of cloud and precipitation overlap for use in general circulation models. *Q. J. Roy. Meteor. Soc.*, **126**, 2525–2544.

Klein, S.A. and C. Jakob, 1999: Validation and sensitivities of frontal clouds simulated by the ECMWF model. *Mon. Wea. Rev.*, **127**, 2514–2531.

Liebe, H. J., Rosenkranz, P., and G. A. Hufford, 1992: Atmospheric 60 GHz oxygen spectrum: New laboratory measurements and line parameters. *J. Quant. Spec. Rad. Trans.*, **48**, 629–643.

Marécal, V., and J.-F. Mahfouf, 2000: Variational retrieval of temperature and humidity profiles

from TRMM precipitation data. *Mon. Wea. Rev.*, **128**, 3853–3866.

Marécal, V., and J.-F. Mahfouf, 2002: Four dimensional variational assimilation of total column water vapor in rainy areas. *Mon. Wea. Rev.*, **130**, 43–58.

Miller, S.D., G.L. Stephens, and A.C.M. Beljaars, 1999: A validation of the ECMWF prognostic cloud scheme using LITE. *Geophys. Res. Lett.*, **26**, 1417–1420.

Morcrette, J.–J., 1991: Evaluation of model-generated cloudiness: Satellite observed and model–generated diurnal variability and brightness temperature. *Mon. Wea. Rev.*, **119**, 1205–1224.

Morcrette, J.–J., E.J. Mlawer, M.J. Iacono, and S.A. Clough, 2001: Impact of the radiation–transfer scheme RRTM in the ECMWF forecasting system. *ECMWF Newsletter*, **91**, 2–9.

Moreau, E., P. Bauer, F. Chevallier, 2002: Microwave radiative transfer modeling in clouds and precipitation. Part II: Model evaluation. *NWP SAF Report No. NWPSAF-EC-TR-006*, 24 pp.

Phalippou, L., 1996: Variational retrieval of humidity profile, wind speed and cloud liquid–water path with the SSM/I: Potential for numerical weather prediction. *Q. J. Roy. Meteor. Soc.*, **122**, 327–355.

Prigent, C., J.R. Pardo, M.I. Mishenko, and W.R. Rossow, 2001: Microwave polarized signatures generated within cloud systems: Special Sensor Microwave Imager (SSM/I) observations interpreted with radiative transfer simulations. *J. Geophys. Res.*, **106:D22**, 28243–28258.

Rizzi, R., 1994: Raw HIRS/2 radiances and model simulations in the presence of clouds. ECMWF Technical Memorandum No. 73, 29 pp. [available from ECMWF, Shinfield Park, Reading RG2 9AX, UK].

Roca, R., L. Picon, M. Desbois, H. Le Treut, and J.–J. Morcrette, 1997: Direct comparison of Meteosat water vapor channel data and general circulation model results. *Geophys. Res. Letters*, **24**, 147–150.

Shah, K.P., and D. Rind, 1995: Use of microwave brightness temperatures with a general circulation model. *J. Geophys. Res.*, **100:D7**, 13841–13874.

Smith, E.A., P. Bauer, F.S. Marzano, C.D. Kummerow, D. McKague, A. Mugnai, G. Panegrossi, 2002: Intercomparison of microwave radiative transfer models for precipitating clouds. *IEEE*

Trans. Geosci. Remote Sens., in press.

Stogryn, A.P., C.T. Butler, and T.J. Bartolac, 1994: Ocean surface wind retrievals from Special Sensor Microwave Imager data with neural networks. *J. Geophys. Res.*, **99:C1**, 981–984.

Sundqvist, H., 1978: A parameterization scheme for non–convective condensation including prediction of cloud water content. *Q. J. R. Meteorol. Soc.*, **104**, 677–690.

Tiedtke, M., 1993: Representation of clouds in large–scale models. *Mon. Wea. Rev.*, **121**, 3040–3061.

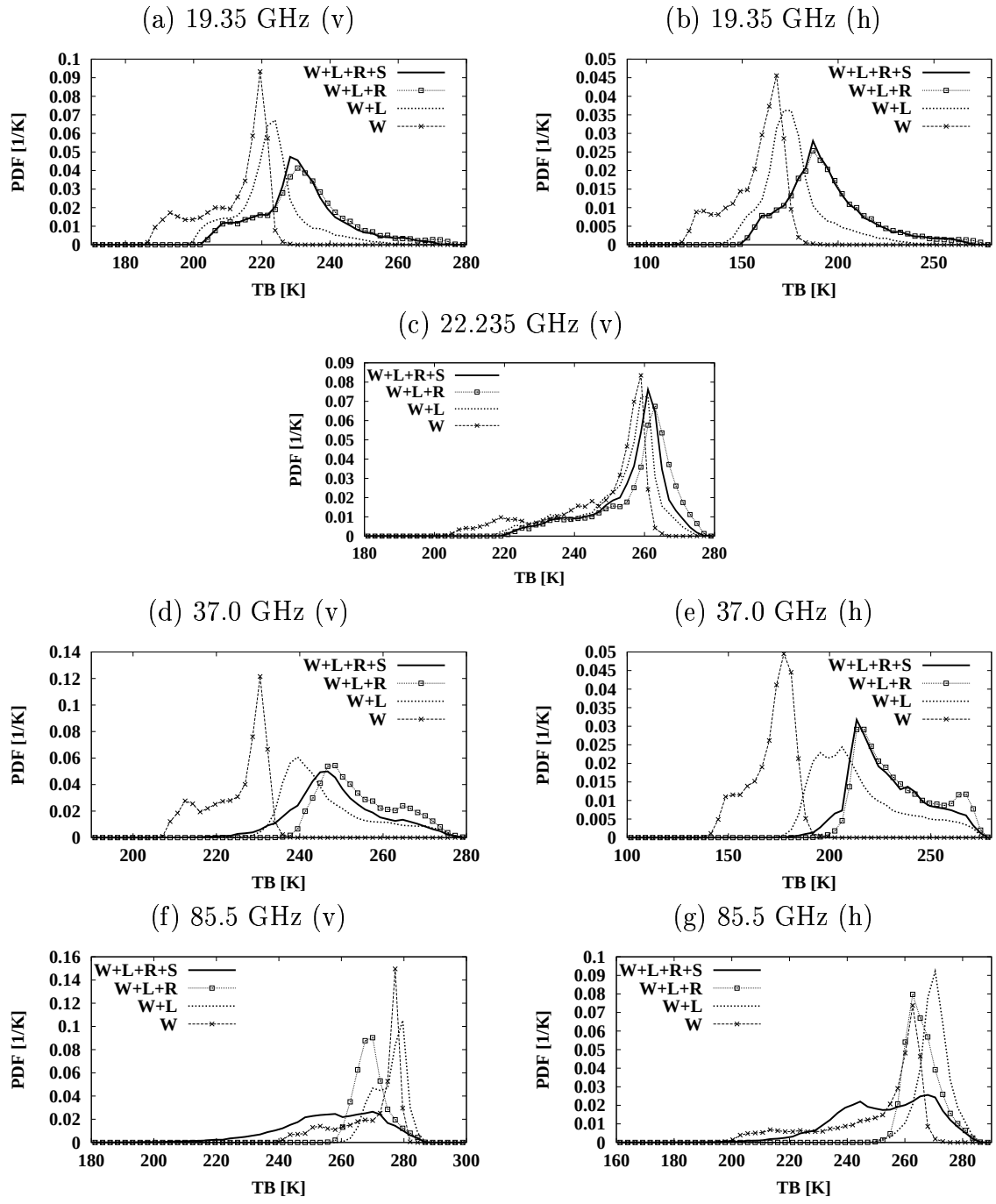

Figure 1: Cumulative impact of water vapor (W), liquid water (L), rain (R), and precipitating snow (S) on the distribution of the computed rain–affected SSM/I TB's. January 1, 2001; 8,232 cases.

(a) January, model

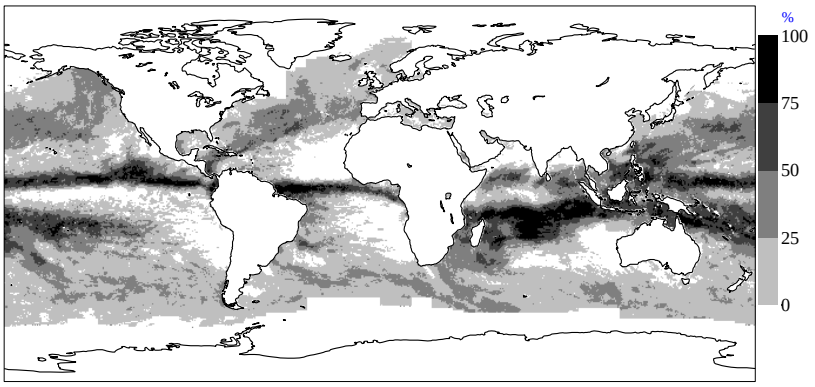

(b) January, observation

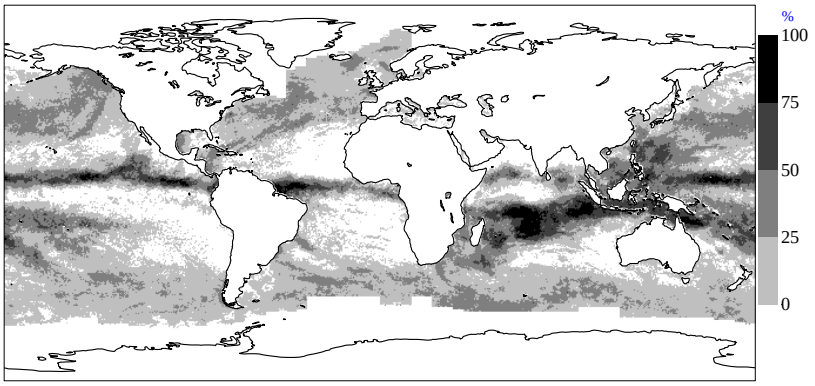

(c) July, model

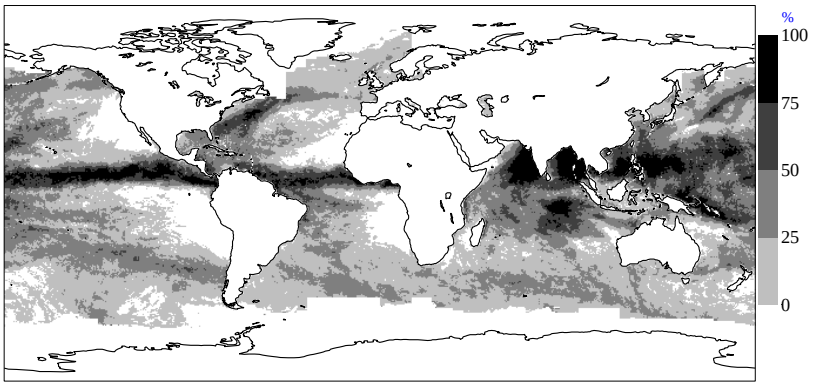

(d) July, observation

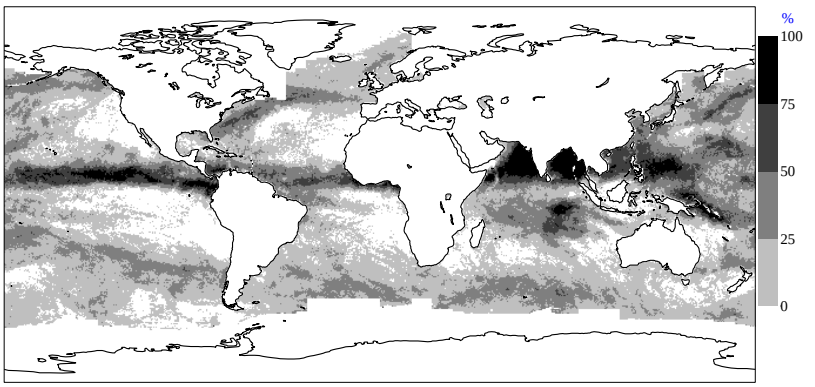

Figure 2: Frequency of occurrence of clouds in the model and in the observations over ocean. Clouds are detected using SSM/I TB's (see text for details).

(a) January, model

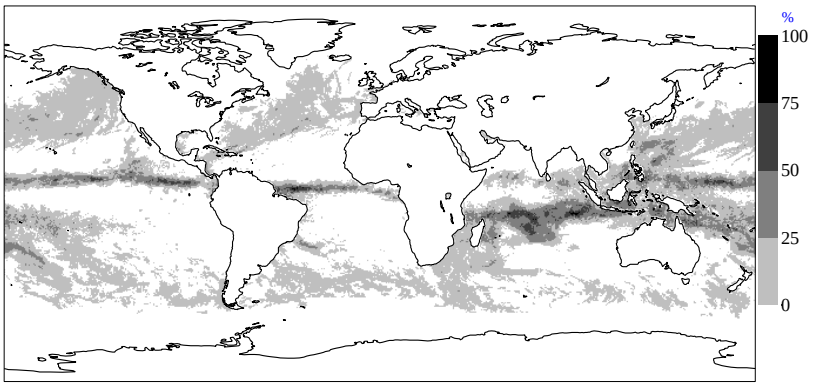

(b) January, observation

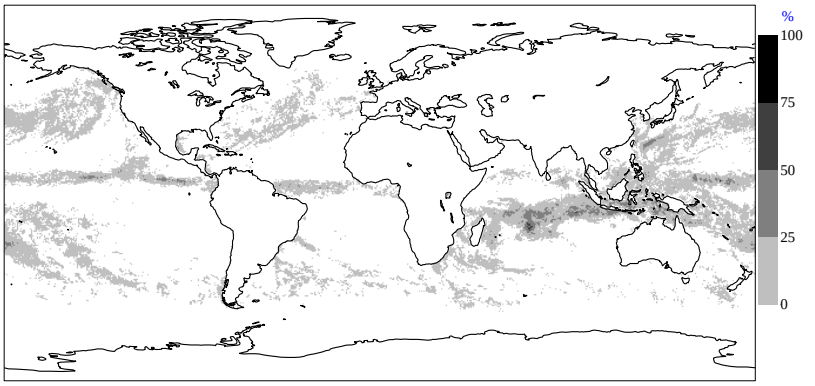

(c) July, model

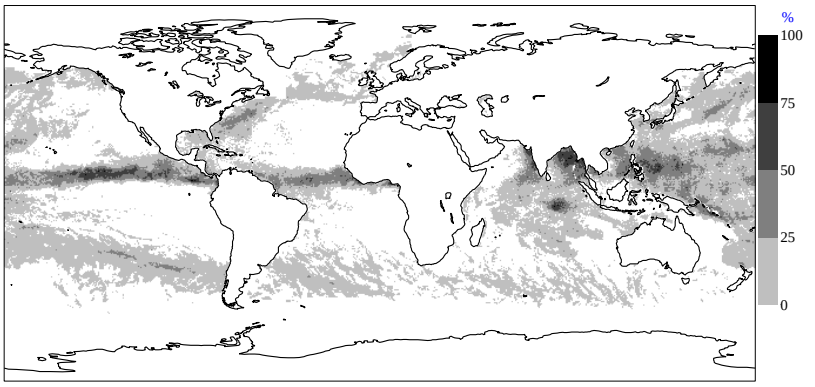

(d) July, observation

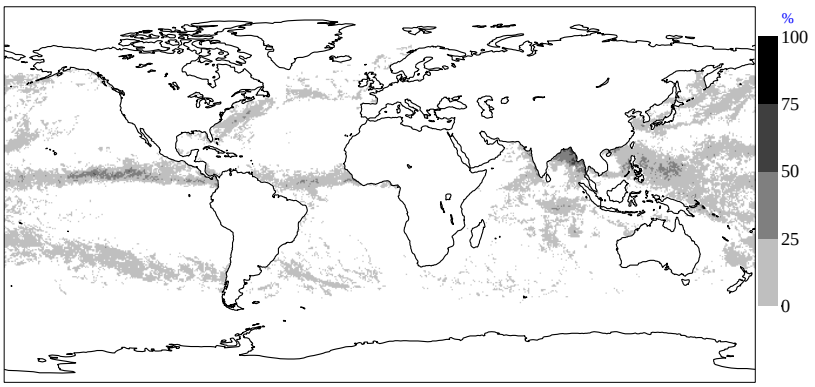

Figure 3: Frequency of occurrence of rain in the model and in the observations over ocean. Rain is detected using SSM/I TB's (see text for details).

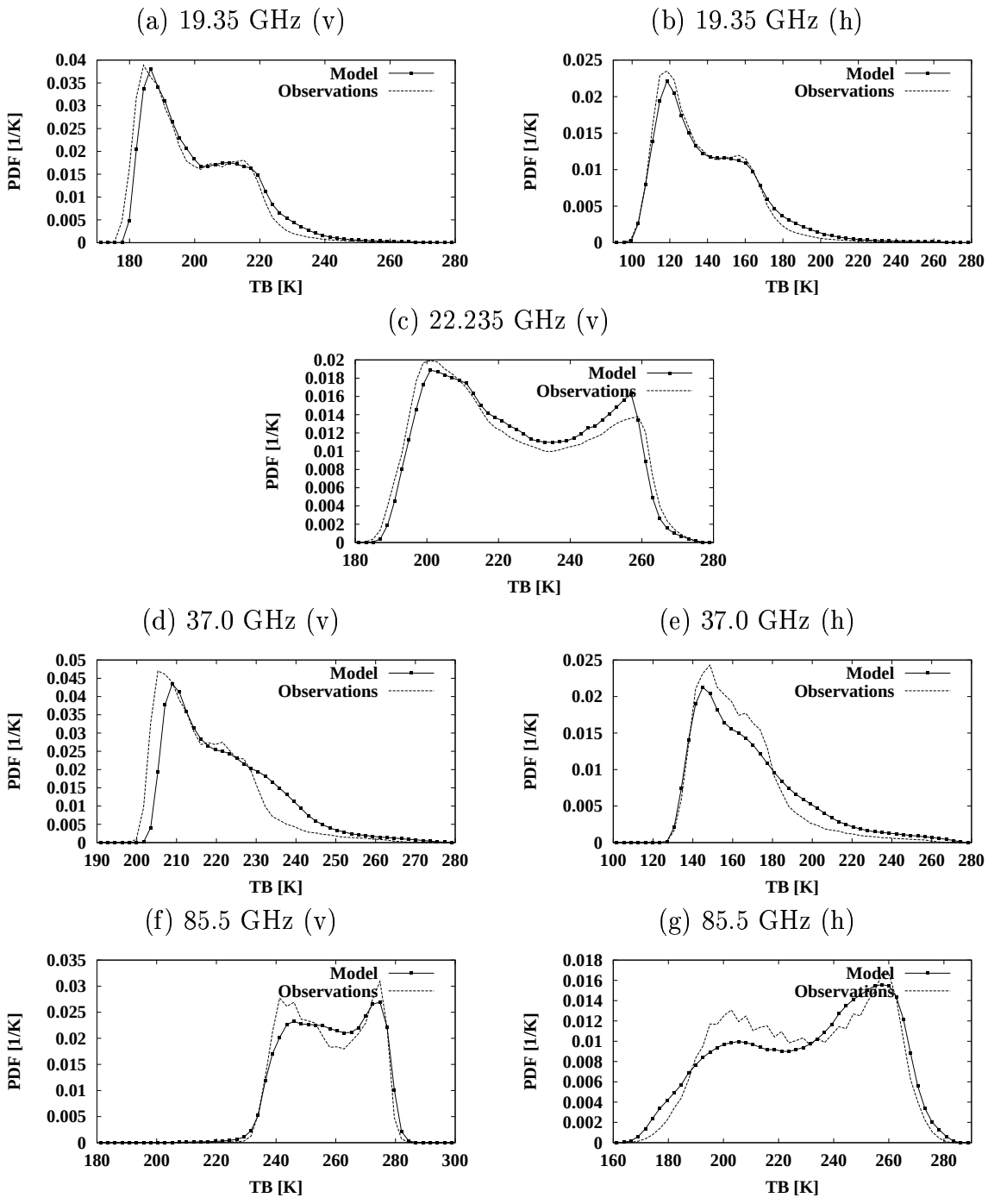

Figure 4: Distribution of the observed and computed SSM/I TB's for grid boxes that are affected by rain in the model or in the observations more than once over the period January 1–15, 2001 (2,638,376 cases).

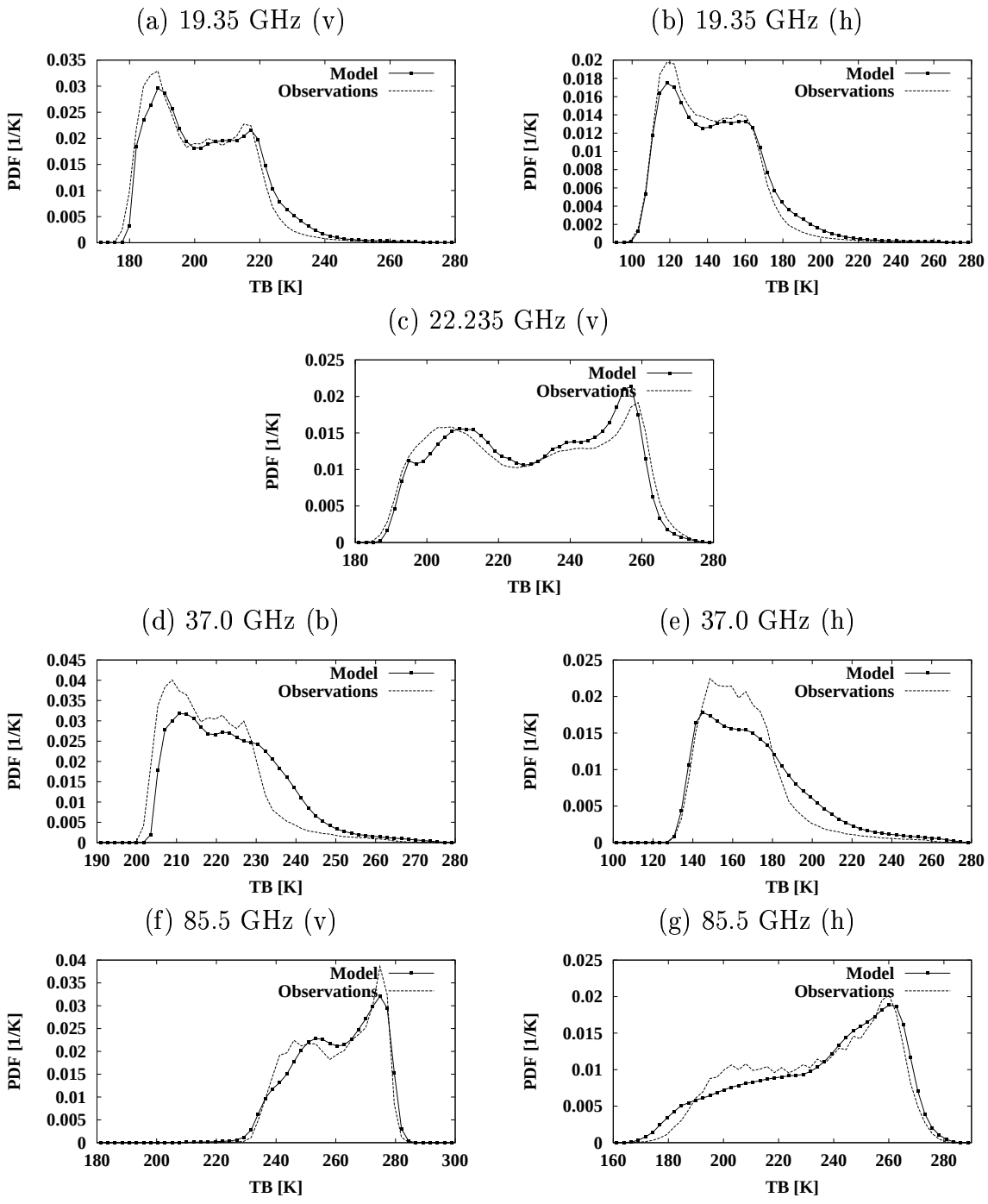

Figure 5: Distribution of the observed and computed SSM/I TB's between July 1–15, 2001 in grid boxes that are affected by rain in the model or in the observations more than once over the period (2,693,167 cases).

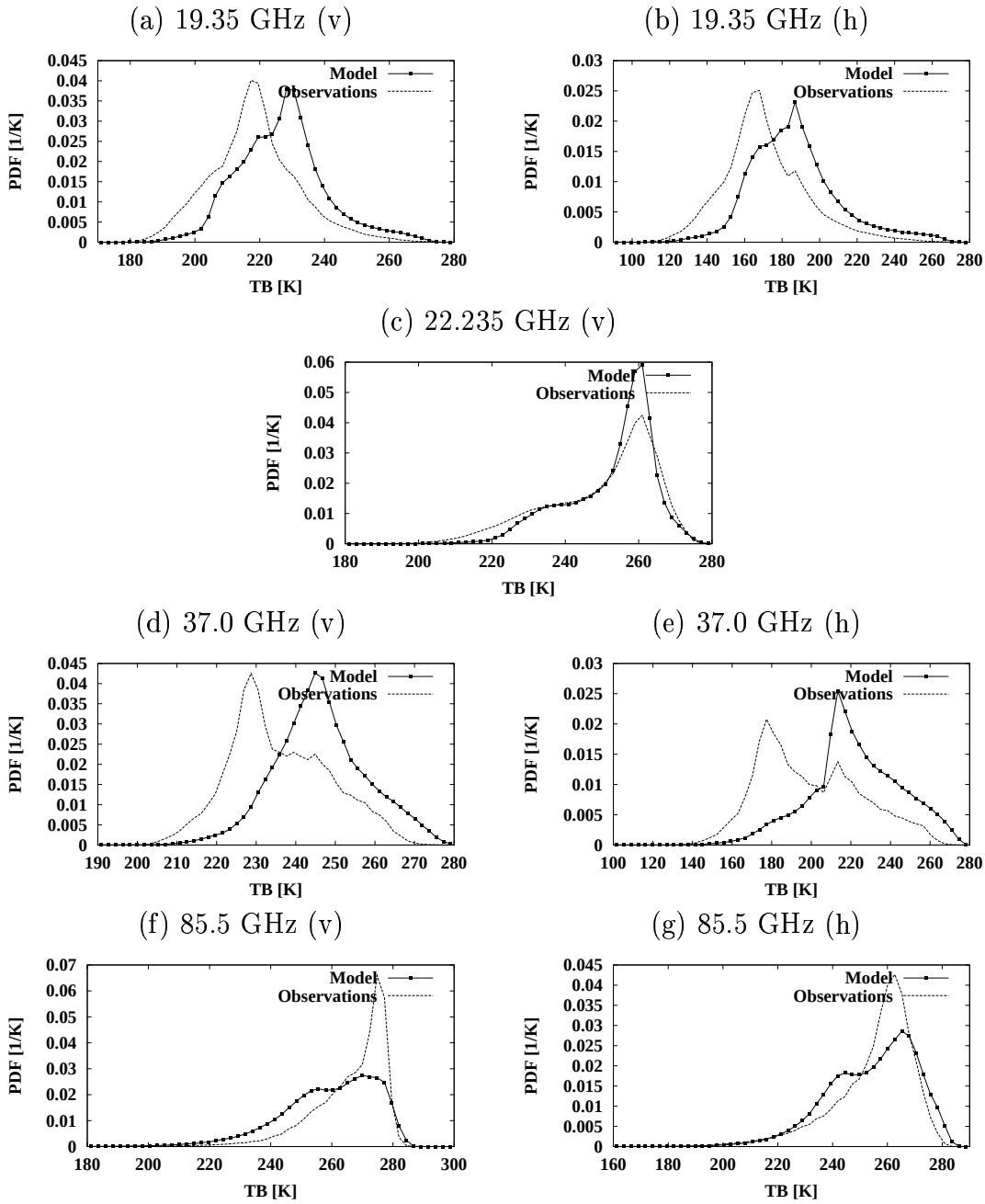

Figure 6: Distribution of the observed and computed SSM/I TB's between January 1 and 15, 2001, when rain was detected in the model or in the observations (304,320 cases).

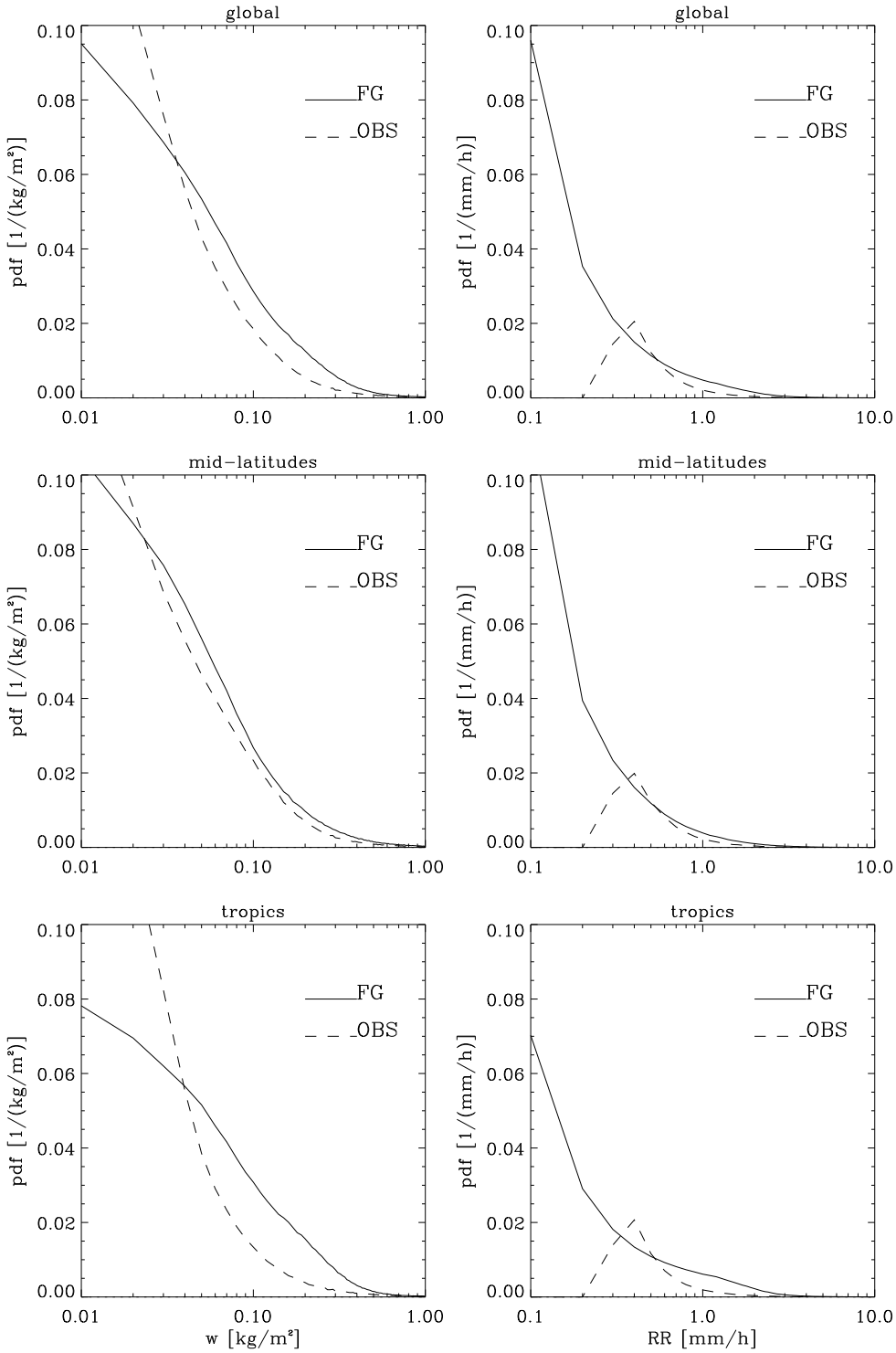

Figure 7: Frequency distribution of model first–guess (solid) vs. retrieved (dashed) cloud liquid water paths (left panels) and surface rainrates (right panels) for January 1–15, 2001.

(a) January 5, model

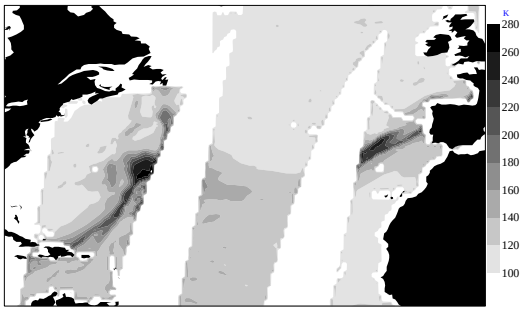

(b) January 5, observations

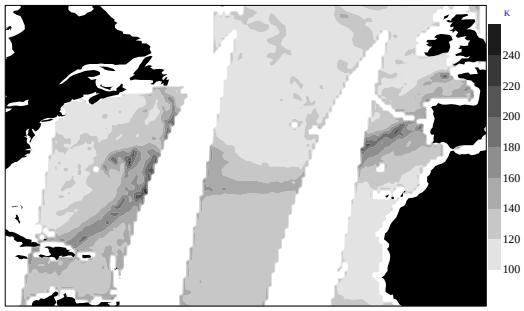

(c) January 7, model

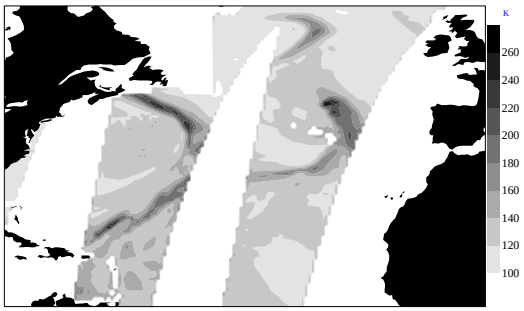

(d) January 7, observations

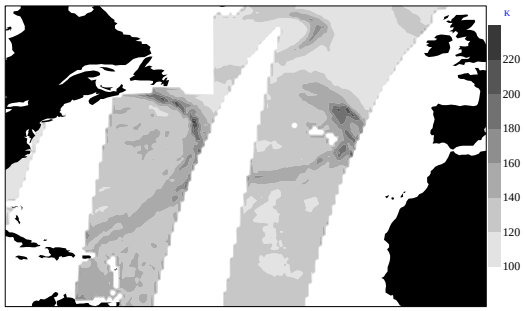

(e) January 14, model

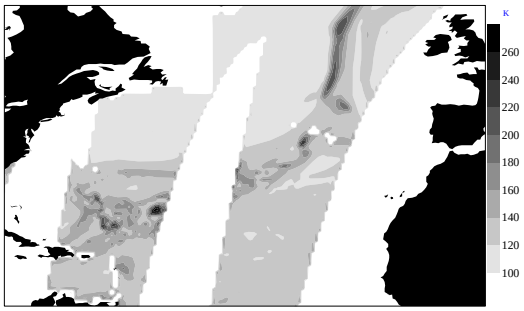

(f) January 14, observations

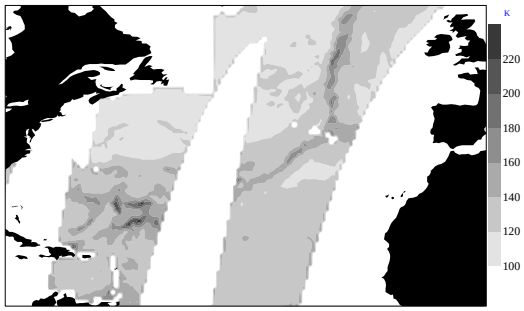

Figure 8: Model and observed 19.35 GHz TB's (horizontal polarization) over the North Atlantic. The data was taken around 12 UTC on the dates shown.

(a) January 2, model

(b) January 2, observations

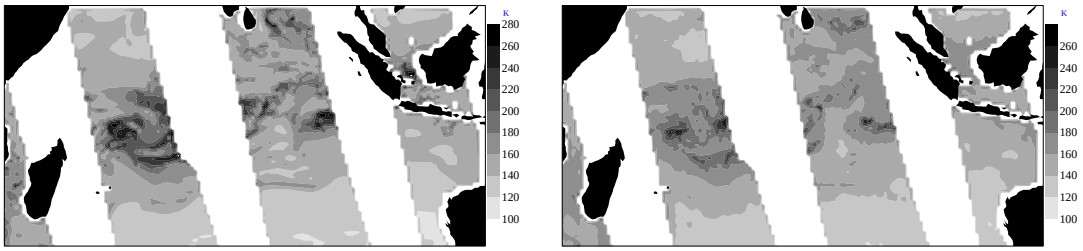

(c) January 7, model

(d) January 7, observations

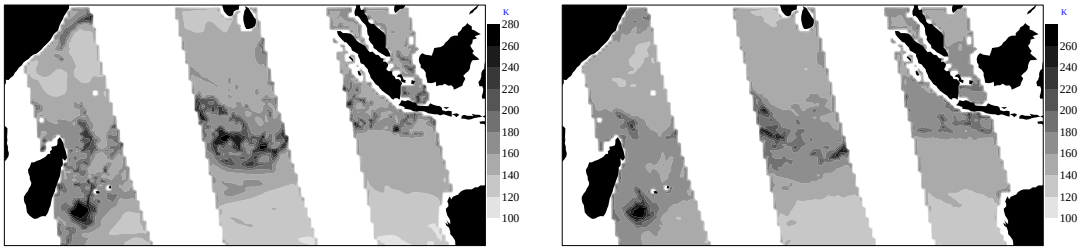

(e) January 11, Model

(f) January 11, observations

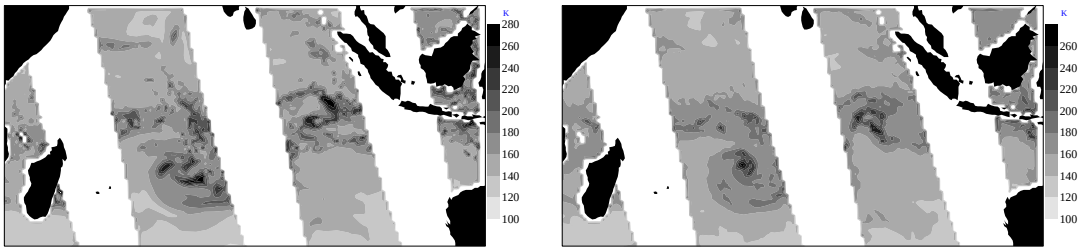

Figure 9: Model and observed 19.35 GHz TB's (horizontal polarization), over the Indian Ocean. The data was taken around 15 UTC on the dates shown.